Soft Matter

PAPER

View Article Online
View Journal | View Issue

Cite this: *Soft Matter*, 2024, **20**, 7021

Anomalous relaxation of coarsening foams with viscoelastic continuous phases†

Chiara Guidolin, *[a] Emmanuelle Rio, [b] Roberto Cerbino, [c] Anniina Salonen [b] and Fabio Giavazzi *[a]

Received 16th May 2024,
Accepted 6th August 2024

DOI: 10.1039/d4sm00588k

rsc.li/soft-matter-journal

We investigate the ultraslow structural relaxation of ageing foams with rheologically tunable continuous phases. We probe the bubble dynamics associated with pressure-driven foam coarsening using differential dynamic microscopy, which allows characterising the sample dynamics in reciprocal space with imaging experiments. Similar to other out-of-equilibrium jammed soft systems, these foams exhibit compressed exponential relaxations, with a ballistic-like linear dependency of the relaxation rate on the scattering wavevector. By tuning the rheology of the continuous phase, we observe changes in the relaxation shape, where stiffer matrices yield larger compression exponents. Our results corroborate recent real-space observations obtained using bubble tracking, providing a comprehensive overview of structural relaxation in these complex systems, both in direct and reciprocal space.

1 Introduction

Jammed soft materials, such as dense emulsions, pastes, foams, and colloidal gels, are ubiquitous in daily life and have numerous industrial applications. Despite their widespread use, these materials often exist out of equilibrium and undergo complex aging processes,[1,2] which are poorly understood and leave a significant gap in knowledge regarding their dynamic properties as they slowly evolve towards equilibrium.

A particularly intriguing feature of these jammed systems is their similarity to molecular glasses.[3] Indeed, the tight packing and/or the presence of strong interactions between the components markedly reduce their mobility, lending the system a glassy dynamical behavior, consisting of very slow relaxations, non-exponential response or correlation functions, history-dependent dynamics, and dynamical heterogeneity.[4]

However, instead of the stretched exponential relaxations and diffusive dispersion relations traditionally found in hard glasses, dynamic light scattering experiments on jammed soft systems often give intermediate scattering functions displaying compressed exponential decays, with an atypical linear dependence of the relaxation rate on the scattering wavevector, reminiscent of ballistic motion.[5] This 'anomalous' relaxation dynamics has been observed in a large variety of disordered, jammed, soft materials, including colloidal fractal gels, concentrated emulsions, micellar polycrystals, and lamellar gels,[6] suggesting the generality of this behavior. More recently, similar dynamics has been spotted even in hard amorphous materials like metallic glasses,[7–10] reporting a temperature-dependent[11] switch from stretched to compressed exponential decays.

This unusual behavior has been ascribed to the relaxation of internal stresses.[12] It was proposed that randomly distributed dipolar stress sources generate displacement fields that lead to directionally persistent displacements characterised by a power-law tailed probability distribution.[6] Several recent modelling studies show that compressed exponential decays can result from elastic responses to local relaxation events within the material.[13–17]

Experimentally, this kind of intermittent stress-driven dynamics has been widely explored in coarsening aqueous foams,[18–24] where the source of stress imbalances can be traced back to the continuous bubble growth and the size of the components lends itself to imaging and light scattering experiments. The pressure-driven coarsening process keeps altering the stress configuration of the system, leading to locally imbalanced stresses that trigger neighbour-switching bubble rearrangements, like those occurring while yielding with external driving. A combined reciprocal and direct space analysis has recently shown how foam dynamics is governed by intermittent bubble displacements exhibiting a persistent direction up to the bubble size length scale.[24] This length scale introduces a cut-off in the probability distribution function of bubble displacements that otherwise exhibits power-law scaling. The existence of such a cut-off length leads to a loss of linearity and the identification of a steeper second low-q regime for the q-dependence of the foam relaxation rate.[24]

[a] *Department of Medical Biotechnology and Translational Medicine, University of Milan, Segrate, Italy. E-mail: chiara.guidolin@unimi.it, fabio.giavazzi@unimi.it*
[b] *Laboratoire de Physique des Solides, Université Paris-Saclay, CNRS, Orsay, France*
[c] *Faculty of Physics, University of Vienna, Vienna, Austria*

† Electronic supplementary information (ESI) available. See DOI: https://doi.org/10.1039/d4sm00588k

While this is known for aqueous foams, what happens in more complex systems is much less understood, even though in many practical applications foams are themselves made from fluids with nontrivial rheology, like gels, emulsions, or pastes. Continuous phase rheology can modify the internal bubble dynamics during coarsening, by slowing down[25,26] or even preventing[27] mutual bubble rearrangements, eventually impacting the overall foam morphology.[28] Stress relaxation thus plays a central role in the long-term foam structure evolution. A deep understanding of bubble dynamics during foam ageing would thus allow for a finer control of foam stability and mechanical properties which is of fundamental importance for many foam applications.

In this study, we examine how the rheological properties of the continuous phase influence the internal structural relaxation of foams during their destabilization. We focus on bubble dynamics within coarsening foams made of concentrated oil-in-water emulsions. At oil volume fractions ϕ beyond random close packing, these dense biliquid dispersions exhibit viscoelasticity, where both the storage modulus and yield stress increase with ϕ.[29,30] Consequently, the rheological properties of the foam continuous phase can be adjusted by altering the emulsion oil fraction.

We have recently shown that higher emulsion yield stresses significantly slow down bubble movement during coarsening by accumulating elastic stresses in the matrix, which decouple bubble growth from dynamics.[27] Nonetheless, the correlation between stress-induced displacements and their signatures in reciprocal space remains largely unexplored. Filling this gap is crucial given that neutron and X-ray experiments on soft jammed materials cannot be easily performed in direct space, and one often relies on reciprocal scale information.

We use differential dynamic microscopy (DDM)[31] to obtain reciprocal space information about the foam relaxation, demonstrating that increasing the emulsion oil fraction modifies the shape of the intermediate scattering function, resulting in more pronounced compressed exponential decay. Furthermore, the lack of bubble rearrangements at high emulsion yield stress[27] is mirrored in reciprocal space by alterations in the q-dependence of the foam relaxation rate. The typically observed superlinear low-q regime in coarsening aqueous foams gradually shifts towards a more linear dispersion relation with increased matrix stiffness, indicative of ultraslow ballistic-like bubble motion.

Our findings elucidate the impact of continuous phase rheology on foam relaxation, as observed in reciprocal space. Moreover, this work provides a detailed analysis of structural relaxation in complex foam systems, representing a foundational study of the interplay between reciprocal and direct space dynamic features potentially extendable to a broad range of soft glassy systems.

2 Materials and methods

2.1 Sample preparation and imaging

Our samples are foams made of concentrated oil-in-water emulsions. Emulsions are first generated by mechanically mixing the oil and aqueous phases using the double-syringe technique. A syringe (Codan Medical, 60 mL) is partially filled with a volume V_{oil} of rapeseed oil (from Brassica Rapa, Sigma Aldrich), while a second one is partly filled with a volume V_{aq} of surfactant solution (sodium dodecyl sulphate, Sigma Aldrich) at 30 g L^{-1} in deionised water. The volumes, V_{oil} and V_{aq}, are chosen according to the desired emulsion oil volume fraction, defined as $\phi = V_{oil}/(V_{oil} + V_{aq})$. The two syringes are then connected with a double luer lock and the syringe plungers are pushed back and forth 30 times. The syringe inlets, having an inner diameter of 2 mm, act as constrictions in the flow of the mixture, breaking the oil phase into micrometric droplets. The final result is a stable emulsion with a droplet volume-weighted diameter distribution centered at around 5 μm, as assessed by laser diffraction granulometry (Mastersizer 3000E, Malvern Panalytical) after emulsion generation. The surface tension of the air/emulsion interface is $\sigma \sim 30$ mN m^{-1}, as measured using a pendant drop tensiometer (Tracker, Teclis, France). The oil fractions investigated are all above the random close-packing fraction and range between 65% and 80%. We thus vary the elastic modulus of the foam continuous phase between 30 and 340 Pa, and its yield stress from 0.5 to 20 Pa.[27,28]

Emulsions are foamed with the aid of a planetary kitchen mixer (Kenwood MultiOne, 1000 W). Freshly generated emulsion is poured into the vessel, and the mixer is operated at an increasing speed until the sample volume increases tenfold. The final foam liquid fraction is measured by weight after generation and is about 11%. The foaming process does not change the drop size distribution of the emulsions, which is stable throughout the experiment, as checked by laser diffraction granulometry. The surfactant concentration in the aqueous phase ensures complete surface coverage of both oil droplets and bubbles at the oil and gas volume fractions considered.

After generation, the foamed emulsion is gently sandwiched between two square glass plates (edge of 20 cm) separated by a rubber gasket with a thickness of 10 mm. The spacing is much larger than the typical bubble size ($R \sim 10^{-1}$ mm), so the cell contains several layers of bubbles, and the foam sample can be safely considered three-dimensional. Nevertheless, what we probe is the dynamics of the bubble layer at the interface between the foam and the top glass plate, which is actually representative of the bulk coarsening.[32,33] Foam ageing is indeed monitored from the top by taking image stacks with a camera (Basler acA3800-14 μm, equipped with a Tamron lens 16 mm F/1.4), while a square array of LED lights provides uniform illumination from above. The effective frame scale is 24.2 pixel mm^{-1}. Images are acquired every 5 seconds (ϕ = 65%, 70%, 75%) or 15 seconds (ϕ = 80%) to ensure proper time resolution for DDM analysis. The emulsion yield stress allows for delaying gravitational drainage[34] so that foam coarsening can be probed in the absence of significant gravity-induced vertical gradients in the liquid fraction.

2.2 Reciprocal space analysis

Bubble dynamics is analysed in reciprocal space using the DDM protocol.[31,35] Raw frames are first cropped around a square

region of interest (2048 × 2048 pixels) in which the illumination is rather uniform. We correct for residual uneven illumination by dividing each frame by a background image obtained by applying a Gaussian filter having a standard deviation of 20 mm from the first frame of the image stack. The width of the Gaussian filter is chosen to be much larger than the typical bubble size but smaller than the extension of the intensity gradient due to uneven illumination.

Since foams are evolving over time, foam dynamics is studied under quasi-stationary conditions[24] by restricting the DDM analysis on three non-overlapping image sub-sequences, centered at different foam ages t^* = 1800, 2700, and 3600 seconds, respectively, and covering a $t^*/4$ time window in which the mean bubble size grows less than 15%.[27]

Each sub-sequence is analysed separately with a custom MATLAB script as follows. The difference between two background-corrected frames acquired at times t and $t + \Delta t$, namely $\Delta I(x, t, \Delta t) = I(x, t + \Delta t) - I(x, t)$, is first calculated for different log-spaced Δt. A 2D fast Fourier transform algorithm is then applied to $\Delta I(x, t, \Delta t)$, and the spatial Fourier power spectra obtained for the same lag time Δt but different reference times t inside the sequence are then averaged. In this way, we obtain the image structure function $d(\mathbf{q}, \Delta t)$, which captures the sample dynamics as a function of the 2D scattering wavevector $\mathbf{q}$ and the lag time Δt. We then exploit the isotropy of the sample to calculate the azimuthal average of $d(\mathbf{q}, \Delta t)$, which provides $d(q, \Delta t)$ as a function of the radial wavevector $q = \sqrt{q_x^2 + q_y^2}$. For each q, the image structure function $d(q, \Delta t)$ is typically a monotonically increasing function of the delay time Δt and is linked to the real part of the intermediate scattering function $f(q, \Delta t)$ by the relation $d(q, \Delta t) = A(q)[1 - f(q, \Delta t)] + B(q)$, where the term $B(q)$ accounts for the camera noise, and the term $A(q)$ is the static amplitude.

By fitting a suitable model to $d(q, \Delta t)$, one can thus extract $f(q, \Delta t)$, whose decay encloses the information on the sample dynamics at a length scale of $2\pi/q$. A function of the type $d(q, \Delta t) = A(q)[1 - f(q, \Delta t)] + B(q)$, where $f(q, \Delta t)$ is a compressed exponential function $f(q, \Delta t) = \exp[-(\Gamma(q)\Delta t)^{\alpha(q)}]$, is then fitted to the image structure function data points for each image sub-sequence. We could fit $d(q, \Delta t)$ to extract both $A(q)$ and $f(q, \Delta t)$. However, since the analysis is restricted to a limited time interval for quasi-stationarity, a full relaxation of $f(q, \Delta t)$ is not observed at all wavevectors q. We thus estimate the amplitude from the time-averaged power spectrum of the single images as $A(q) \simeq 2\,\langle|\hat{I}(q)|^2\rangle - B(q)$,[36,37] where $B(q)$ is the noise level estimated from a first unconstrained fit of $d(q, \Delta t)$. This approximation is justified as the optical signal due to the foam is much higher than any other contribution coming from stray light or dirt on the optical components. We first fit $d(q, \Delta t)$ normalising with the static amplitude $A(q)$ but leaving the compressing exponent α as a free parameter to check its dependence on q. The compressing exponent is not expected to significantly vary over the range of q considered, according to previous work on aqueous foams.[24] The obtained compressing exponents $\alpha(q)$ are indeed almost constant, displaying a weak q-dependence only for larger ϕ values (ESI,† Fig. S1). We thus evaluate the average compressing exponent $\alpha = \langle\alpha(q)\rangle$, and perform a more constrained fit of $d(q, \Delta t)$, fixing the compressing exponent to be equal to its mean value α. In this way, we keep the functional form of the intermediate scattering function constant over the range of q, and we can safely extract a consistent scaling of the relaxation rate $\Gamma(q)$ from the decay of $f(q, \Delta t)$.

As the compressing exponent α is found to change with the oil fraction ϕ, when comparing the relaxation rates between samples, we consider an average value of $\Gamma(q)$ to make it less dependent on the specific shape of the decay. For better consistency, the values of $\Gamma(q)$ obtained from the fit are thus corrected to compensate for the variations in the compressing exponent by considering the general following relation for the average characteristic time of decay τ: $\bar{\tau} = \int_0^\infty e^{-(t/\tau)^\alpha} dt = \frac{\tau}{\alpha}\mathbf{\Gamma}\left(\frac{1}{\alpha}\right)$, where $\mathbf{\Gamma}$ denotes Euler's gamma function. The average relaxation rate is then estimated as $\bar{\Gamma} = 1/\bar{\tau} = \Gamma(q)\alpha \Big/ \mathbf{\Gamma}\left(\frac{1}{\alpha}\right)$.

2.3 Direct space analysis

Real-space image processing is performed as described in previous work.[27] Briefly, raw foam images are processed with custom MATLAB scripts as follows. After background correction, the same images used for DDM analysis are segmented with adaptive thresholding and then skeletonised with a watershed algorithm. The typical number of detected bubbles is always larger than 10^3 at each foam age, ensuring good statistics. The size of each bubble is estimated from the foam skeleton as the radius $R = \sqrt{A/\pi}$, where A is the area of the polygonal cell outlining the bubble boundaries. The average bubble size at a given foam age t^* is then calculated as the ensemble mean bubble radius of the corresponding frame, namely $R^* = \langle R\rangle$.

Bubble dynamics is then characterised in real space at different foam ages t^* by performing bubble tracking using TrackMate[38,39] on the segmented foam images within the time window considered for quasi-stationarity. Only bubbles whose trajectories cover the whole time window are kept for analysis, whereas small bubbles that disappear due to coarsening are discarded. The latter, however, correspond to less than 20% of the total number of detected bubbles.

3 Results and discussion

Foams age *via* gas diffusion from smaller bubbles to larger ones, driven by the differences in their Laplace pressures.[40] This pressure-driven coarsening process causes the mean bubble size to increase over time until complete phase separation.[41] Bubble size variations continuously generate stress imbalances within the foam, which eventually relax through local bubble rearrangements involving an exchange of neighbours.[42]

The systems under study are foams made of air bubbles tightly embedded in concentrated oil-in-water emulsions. We recently showed that the presence of a viscoelastic emulsion between the bubbles strongly affects the long-term coarsening evolution[28] as well as the associated internal bubble dynamics.[27] Indeed, our previous studies revealed that, at low emulsion oil fractions, such systems behave like aqueous foams: bubbles freely rearrange during coarsening so that they move persistently in one direction only up to a critical length scale of the order of the bubble size.[27] By contrast, the increase of the emulsion yield stress strongly hinders mutual bubble displacements, as the emulsion can bear stresses coming from bubble size variations up to its yielding point.[27] The lack of bubble rearrangements prevents sudden changes in the direction of the bubble trajectories: bubbles keep moving persistently, deforming the material without relaxing the accumulated stress *via* neighbour-switching events. While our previous work was purely based on a real-space analysis and description of the internal bubble dynamics, here, we investigate how the observed change in the bubble mobility is reflected in the reciprocal space.

3.1 DDM captures the coarsening-induced relaxation dynamics

We perform differential dynamic microscopy on the same foam systems by varying the emulsion oil fraction ϕ between 65% and 80%. For each sample, we probe the bubble dynamics at three different foam ages t^* corresponding to 1800, 2700, and 3600 seconds. A typical foam appearance is shown in Fig. 1(a) for ϕ = 65%. At each foam age, we compute the intermediate scattering function $f(q, \Delta t)$. A few representative examples, calculated at different wavevectors q, are shown in Fig. 1(b) for the sample ϕ = 65% at age t^* = 3600 s, but extended results can be found in ESI† (Fig. S2–S4). The intermediate scattering function $f(q, \Delta t)$ shifts towards a smaller Δt with increasing q, reflecting the slower relaxation of larger length scales.

As we restrict the determination of $f(q, \Delta t)$ to a time window over which the foam can be considered quasi-stationary, the accessible data range is limited, and a full decay is only obtained for large q-values. Despite this limitation, we can access the decay rate of $f(q, \Delta t)$ by fitting these curves to a model function. However, we restrict our analysis to those wavevectors for which at least the first 10% of decay is visible.

The curves are well fitted with a compressed exponential function of the type $f(q, \Delta t) = \exp[-(\Gamma(q)\Delta t)^{\alpha}]$, as in shaving foam,[24] with a compressing exponent $\alpha \simeq 1.35$. The corresponding foam relaxation rate $\Gamma(q)$ obtained for the sample ϕ = 65% at different foam ages is shown in Fig. 1(c). The curves shift downwards with time, mirroring the slowdown of the bubble dynamics as the foam coarsens. At each foam age, two distinct dynamic regimes are observed, as reflected by two different slopes in $\Gamma(q)$: at high q, the dispersion relation is linear; at low q, the relaxation rate exhibits a steeper q-dependence. A similar behavior was observed for shaving foam, where the dispersion relation was found to turn from a linear to a power-law scaling $\Gamma(q) \sim q^{\beta}$ (with $\beta > 1$) for wavevectors corresponding to length scales above the typical bubble size.[24] In shaving foam, the high-q linear scaling has been ascribed to the ballistic-like bubble motion under the strain field induced by stress imbalances within the foam. The occurrence of bubble rearrangements suddenly changes the local stress configuration, causing a loss of directional persistence in real space, which is mirrored by the change in slope to a stronger q-dependence of $\Gamma(q)$ at low q. This picture also holds for the foamed emulsion at ϕ = 65%, as real-space bubble motion resembles that of shaving foam.[27] Moreover, the crossover between the two regimes occurs at a wavevector $q^* = 2\pi/R^*$, corresponding to the typical bubble size R^* and shifts towards smaller q over time, consistent with the gradual increase of R^*

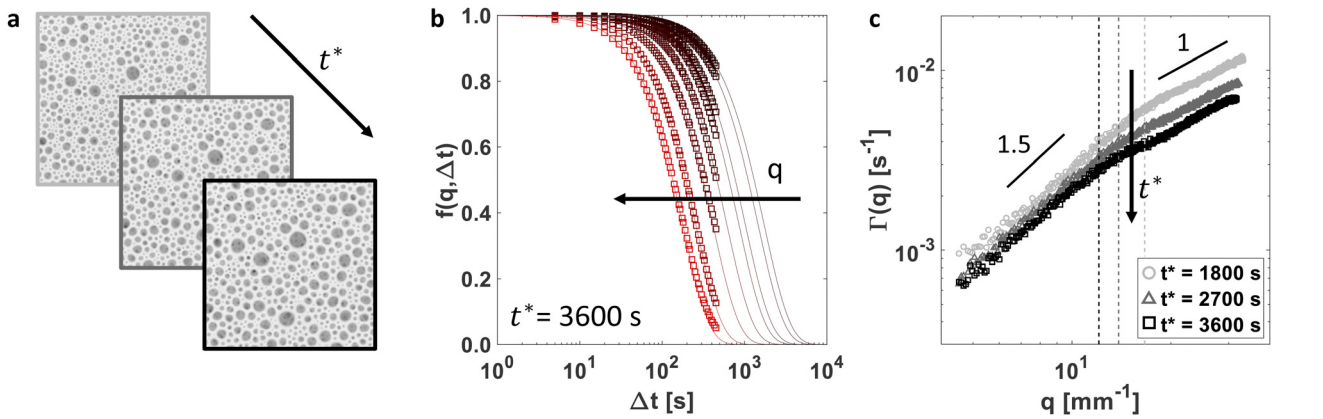

Fig. 1 DDM of coarsening foamed emulsions. (a) Representative images of the foamed emulsion at ϕ = 65% at foam ages t^* = 1800, 2700, and 3600 seconds. Bubbles appear as dark spots embedded in the whitish emulsion, forming a foam continuous phase. Each photo represents only a portion corresponding to 1/16th of the total image used for the analysis. The edge is 21 mm. (b) Representative curves of the intermediate scattering function $f(q, \Delta t)$ obtained at different wavevectors q for the sample ϕ = 65% at t^* = 3600 s. Experimental data are represented by empty symbols, while the corresponding compressed exponential fits are shown with solid lines. (c) Relaxation rate $\Gamma(q)$ obtained for the same sample at increasing foam ages t^* of 1800 s, 2700 s, and 3600 s. The vertical dashed lines highlight the wavevectors $q^* = 2\pi/R^*$, corresponding to characteristic bubble sizes.

as the foam ages. At low ϕ, coarsening foamed emulsions thus share the same dynamic features as classic aqueous foams in both real and reciprocal spaces.

3.2 The relaxation dynamics depend on matrix elasticity

We now repeat the same analysis for samples with different oil fractions. At each foam age, the shape of the intermediate scattering function becomes more compressed with a stiffer emulsion, as reflected by the increase of the compressing exponent α with increasing ϕ, as shown in Fig. 2(a). The corresponding relaxation rates are compared in Fig. 2(b) for the same foam age $t^* = 3600$ s. The comparison reveals that $\Gamma(q)$ decreases with increasing oil fraction, reflecting a slowing down of coarsening-induced dynamics. We stress that this slowing down is not due to any difference in the coarsening rate $\dot{R} = \mathrm{d}R/\mathrm{d}t$, as the latter does not change between the samples, as shown in previous work.[27] The reduction can thus be entirely ascribed to the change in the continuous phase rheology.

Remarkably, the q-dependence of $\Gamma(q)$ also changes with ϕ. We can see that, while at a low ϕ, one can clearly distinguish two distinct dynamic regimes, such a distinction is gradually lost as ϕ is increased up to 80%, where $\Gamma(q)$ almost exhibits a single ballistic-like scaling over the whole range of accessible wavevectors. A power-law fit of $\Gamma(q)$ in the low-q regime (i.e. for $q < 2\pi/R^*$) indeed reveals that the exponent β decreases with increasing ϕ heading towards linear scaling. As discussed in previous work,[24] the low-q regime is directly linked to the presence of the cut-off length: if the probed length scale exceeds the largest bubble displacement, the intermediate scattering function can still be described by a compressed exponential with the same exponent α, but with a relaxation rate obeying a different dispersion relation $\Gamma(q) \sim q^{\beta}$, with $\beta = 2/\alpha$. Our results are in good agreement with this prediction, as shown in Fig. 2(c).

Thus, in foamed emulsions, compressed exponential relaxations are associated with a high-q linear dispersion relation combined with a steeper low-q regime whose q-dependence changes ϕ according to the variation in the compressing exponent α.

We now focus on the high-q linear scaling of $\Gamma(q)$. On length scales below the bubble size, namely at $q > 2\pi/R^*$, the

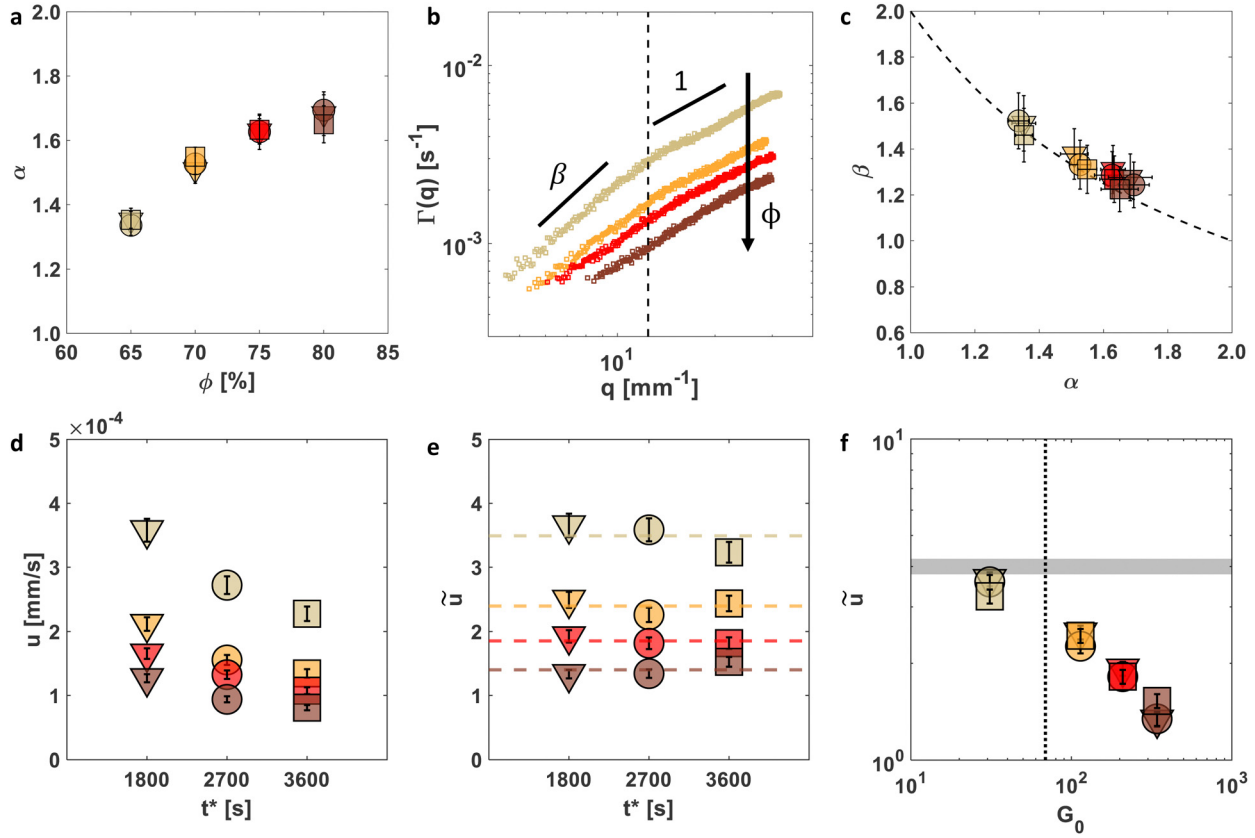

Fig. 2 Foam relaxation at different continuous phase elasticities. (a) Compressing exponent α for samples at different oil fractions ϕ and foam ages t^* = 1800 s (triangles), 2700 s (circles), and 3600 s (squares). (b) Relaxation rates $\Gamma(q)$ obtained for different ϕ values at fixed foam age $t^* = 3600$ s. The slope β highlights the super-linear scaling of the low-q regime ($q < q^*$). The vertical dashed line marks the crossover wavevector $q^* = 2\pi/R^*$. (c) Comparison between exponents β and α. The dashed line corresponds to the expected relation $\beta = 2/\alpha$. (d) Velocity u obtained from a linear fit of the type $\Gamma(q) = uq$ in the high-q regime ($q > q^*$) for different foamed emulsions at different foam ages t^*. (e) Same velocities after normalisation with the coarsening rate, namely $\tilde{u} = u/\dot{R}$. (f) Variation in normalised velocity $\tilde{u}$ with emulsion elasticity. The vertical dashed line marks the critical elastic modulus $G_0^* \sim \sigma/R$. The horizontal bar marks the reference value of $\tilde{u}$ measured for shaving foam.[24]

relaxation rate can be expressed as $\Gamma(q) = uq$, with u representing a characteristic relaxation velocity. At a fixed foam age, the downward shift of $\Gamma(q)$ with increasing ϕ observed in Fig. 2(b), thus reflects a decrease of u.

For a given foam sample, $\Gamma(q)$ decreases with increasing foam age, reflecting the slowing down of the coarsening kinetics over time, as well as the characteristic velocity u, as shown in Fig. 2(d). For a coarsening aqueous foam, previous work revealed that the dispersion relations $\Gamma(q)$ obtained at different foam ages collapse onto a single master curve after rescaling q with the bubble size R and Γ with the strain rate $\dot{R}/R$ associated with coarsening.[24] This means that the characteristic velocity u normalised with the coarsening rate $\dot{R} = \mathrm{d}R/\mathrm{d}t$, namely $\tilde{u} = u/\dot{R}$, remains constant over time over a large range of bubble sizes. In our samples, the normalised velocity $\tilde{u}$ does not display a significant variation over time, as shown in Fig. 2(e), and can thus be considered constant at least within the range of bubble sizes investigated (as t^* is doubled from 1800 s to 3600 s, we register a $\sim$40% increase of R^* from 0.37 to 0.51 mm).

As the coarsening rate at a given foam age is essentially the same for all samples, the observed variation in u, and hence of $\tilde{u}$, with ϕ can be entirely ascribed to the different rheology of the foam continuous phase.

A key observation linking the continuous phase rheology to the observed dynamics is that the linear scaling of $\Gamma(q)$ is found at high values of q corresponding to length scales that are much smaller than the typical bubble size. Bubble displacements over such short length scales are too small to make the interstitial emulsion yield[27] and are, therefore, expected to correspond to the elastic deformations of the foam matrix. Motivated by this observation, we expect the high-q bubble dynamics to be governed by continuous phase elasticity. We thus plot the characteristic velocity $\tilde{u}$ as a function of the emulsion elastic modulus G_0 in Fig. 2(f). In the same graph, we also plot the value of $\tilde{u}$ calculated for shaving foam[24] as a horizontal bar. Even though this value does not depend on the bubble size,[24] it could, in principle, depend on the foam liquid fraction. However, we emphasize that the shaving foam has a liquid fraction ($\sim$8%) that is very close to that of our samples ($\sim$10%). We can thus consider its value of $\tilde{u}$ as a reference value for an equivalent aqueous foam having $G_0 \sim 0$. From the graph, we can see that the normalised velocity for the sample with the lowest G_0 is very close to that expected for an equivalent aqueous foam. By contrast, a gradual reduction of $\tilde{u}$ is observed with increasing emulsion elasticity.

In principle, the matrix elasticity is expected to affect foam coarsening once the elastic modulus G_0 overcomes the bubble capillary pressure σ/R (σ is the matrix surface tension and R is the typical bubble size), namely when the so-called elastocapillary number[43,44] $\mathrm{Ca_{el}} = G_0R/\sigma$ becomes larger than one.‡ We can, therefore, estimate a critical elastic modulus G_0^* corresponding to $\mathrm{Ca_{el}} \simeq 1$, above which we expect the continuous phase elasticity to start impacting the foam relaxation dynamics. Using $\sigma \simeq 30$ mN m^{-1} and an average bubble radius $R \simeq 0.44$ mm, we find $G_0^* \simeq 68$ Pa, which is highlighted in Fig. 2(f) as a vertical dashed line. We can see that our data consistently show a significant deviation from the aqueous foam behavior only at G_0 above G_0^*, while the sample at ϕ = 65% having $G_0 < G_0^*$, behaves akin to an aqueous foam.§ Moreover, we stress that the dependence of $\tilde{u}$ on G_0 can be considered as the Fourier-space manifestation of the decoupling between bubble growth and mobility observed in the real space in previous work.[27]

3.3 Direct space analysis corroborates DDM results

We remark that the observation of a ballistic-like scaling of the relaxation rate is *a priori* compatible with different microscopic scenarios, including the presence of a spatially correlated flow[45] or even a global drift,[46] as well as the independent persistent motion of single particles.[47] For our systems, real-space bubble tracking performed in previous work already revealed the presence of persistent bubble motion over short length scales.[27] To better understand the real-space meaning of the characteristic velocity u obtained in our Fourier space analysis, we exploited the bubble trajectories. We first check for the presence of possible correlations in bubble motion. We start by looking at whether and how the mobility of individual bubbles depends on their radius R. Only a mild dependence of the single-bubble mean square displacement on R is observed in our system (ESI,† Fig. S5(b)), not compatible with the scaling $\mathrm{MSD} \propto R^{-1}$ recently reported for a dense ripening emulsion.[48] Moreover, the spatial correlation properties of the displacement field are surprisingly similar between the samples and do not suggest the presence of long-range coordination in the bubble motion (ESI,† Fig. S5(c)).

At each foam age t^*, the probability distribution of bubble displacements systematically shifts to larger displacements with increasing time delay Δt at both low and high ϕ, as pointed out in ref. 27 and shown in the ESI† (Fig. S6–S8). The position of the distribution peak grows linearly over time, with the velocity u_p matching the characteristic velocity u obtained from the DDM analysis, as shown in Fig. 3(a). The observed distribution shift is thus fully consistent with the persistent bubble motion with a typical velocity u. Indeed, a simple normalisation of both x and y axes with Δt leads to excellent data collapse, as shown in Fig. 3(b) for ϕ = 65% at t^* = 3600 s.

‡ We remind that the limit $\mathrm{Ca_{el}} \to 0$ corresponds to the case of a purely viscous continuous phase ($G_0 \sim 0$), *i.e.*, an aqueous foam, whereas $\mathrm{Ca_{el}} \to +\infty$ corresponds to the limit of a solid, thus static, foam.

§ We note however that the critical value G_0^* depends on the bubble size. For smaller bubble radii, G_0^* shifts to higher values, extending the range of elastic moduli G_0, where we can still expect a classic foam behaviour. By contrast, G_0^* decreases for larger bubbles, meaning that we can observe a deviation from traditional coarsening at much lower values of G_0. In a coarsening foam, the mean bubble size grows over time, meaning that emulsion elasticity gradually becomes more and more important compared to bubble capillarity. The dependency of $\tilde{u}$ on G_0 is thus expected to vary over time. However, the onset of heterogeneous coarsening at larger bubble sizes leads to local structural changes that prevent a simplified description of sample dynamics.

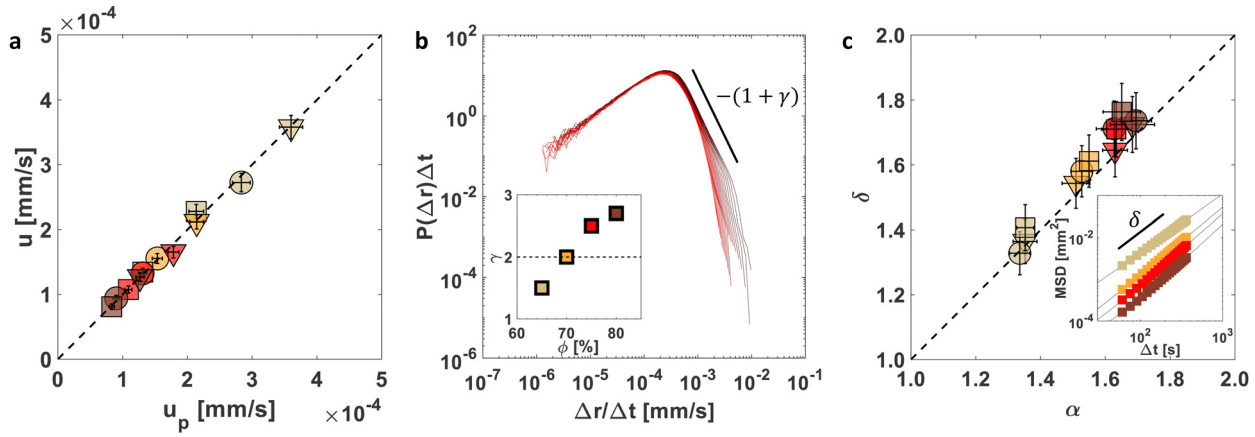

Fig. 3 Real-space bubble displacements. (a) Comparison between the characteristic velocity u obtained using DDM and the velocity corresponding to the peak of the bubble displacement distribution u_p calculated using bubble tracking. (b) Rescaled probability distribution functions of bubble displacements at different delays Δt (color code going from black to red with increasing lag time) for the sample ϕ = 65% at a foam age t^* = 3600 s. The inset shows how the exponent γ varies with ϕ, exceeding the limit γ = 2, as marked by the horizontal dashed line. (c) Comparison between the exponent δ measured from the power-law Δt dependence of the MSD (inset from ref. 27) and the compressing exponent α measured from the intermediate scattering functions. The dashed line corresponds to the expected relation $\delta = \alpha$. Different colours correspond to different ϕ and different symbols for different foam ages t^*, as indicated above.

Substantially equivalent results obtained at different foam ages and oil fractions are reported in ESI† (Fig. S6–S8).

This normalisation highlights a power-law decay of the distributions at bubble displacements right above the maximum before sharply dropping at the cut-off. The probability density function is observed to decay as $P(\Delta r, \Delta t)\Delta t \sim (\Delta r/\Delta t)^{-(\gamma+1)}$, with exponent γ increasing with ϕ, as shown in Fig. 3(b).

We recall that the compressed exponential relaxations of the intermediate scattering function imply the presence of power-law tails in the probability density function of particle displacements. Indeed, intermediate scattering functions decaying as $f(q, \Delta t) = e^{-(\Gamma(q)\Delta t)^{\alpha}}$, with $\Gamma(q) \sim q$, imply the probability density function of displacements decaying as $P(\Delta r, \Delta t) \sim \Delta r^{-(\alpha+1)}$ at large Δr. This is because the Fourier transform of a compressed exponential function is a Levy stable distribution, which displays a power-law tail for large values of its argument.

However, the values of γ obtained for $\phi > 65\%$ are well above the expected value $\gamma = \alpha$ and even exceed the asymptotic limit of the Gaussian distribution γ = 2. This apparent discrepancy can be safely ascribed to finite sampling.[49] Indeed, a significant overestimation of the tail exponent in finite samples can arise for compressing exponents α above $\simeq$1.5, as the Levy stable distribution develops a first steeper decay right past the maximum peak before reaching the asymptotic decay with the correct exponent only at larger arguments.[49] The expected matching between γ and α can thus be directly checked only for ϕ = 65%. However, for larger ϕ, the experimental exponents γ are in good agreement with the values calculated for the apparent steeper decay expected for similar compressing exponent α (ESI,† Fig. S9). We note that the observation of the exact asymptotic power-law tail at high ϕ is, in our case, prevented by the presence of the cut-off length that physically limits the maximum bubble displacement.

If we now consider the bubble mean square displacement (MSD), defined as $\langle \Delta r^2 \rangle = \int_0^{+\infty} r^2 P(r, \Delta t) dr$, when the compressing exponent α is smaller than 2, the MSD is infinite for every Δt. However, the presence of a cut-off length avoids this unphysical situation; with such a cut-off, the MSD is expected to scale as a power law $\sim \Delta t^{\delta}$, with an exponent δ equal to the compressing exponent α.[24] Experimentally, a scaling MSD $\sim \Delta t^{\delta}$ is observed for each sample, with the exponent δ increasing with ϕ and gradually approaching the value 2 compatible with ballistic-like bubble motion.[27] As shown in Fig. 3(c), the exponent δ is in good agreement with the compressing exponent α obtained from the fit of the intermediate scattering function.

Overall, we find that changing the continuous phase rheology strongly modifies the structural relaxation of the coarsening foams. Ballistic-like bubble displacements at small length scales are observed in samples with very different matrix rigidities. Increasing the emulsion elasticity causes a reduction in the characteristic velocity associated with this bubble motion, as consistently observed in both direct and reciprocal space. Qualitative differences arise at larger bubble displacements, with emulsion plasticity governing the maximum extent of persistent displacements. Increasing the emulsion yield stress hinders mutual bubble displacements, affecting the overall shape of the bubble displacement distributions. This results in steeper scaling of the mean square displacement with increasing matrix stiffness, which translates into larger compressing exponents in the reciprocal space.

4 Conclusions

In this work, we investigated the internal dynamics associated with pressure-driven coarsening in foams made of dense emulsions. The use of differential dynamic microscopy allowed

unprecedented characterisation of bubble dynamics in the reciprocal space for such complex foams with simple imaging experiments. Like many other disordered non-equilibrium systems,[6] foamed emulsions exhibit compressed exponential relaxations associated with a ballistic-like linear dependency of the relaxation rate on the scattering wavevector.

We showed that changing the continuous phase rheology affects the shape of the intermediate scattering function, with stiffer emulsions yielding more compressed exponential decay. Our work thus unveils the possibility of changing the foam relaxation features by just modifying the rheological properties of the material between bubbles.

DDM results are also in excellent agreement with real space observations obtained with bubble tracking, providing a robust link between direct and reciprocal space and significantly contributing to the understanding of internal stress-driven bubble dynamics.

As in coarsening aqueous foams,[24] the linear scaling of the foam relaxation rate is lost at a critical wavevector corresponding to the bubble length scale; the occurrence of bubble rearrangements within the foam suddenly changes the local stress configuration causing a loss of directional persistency in the bubble motion.

Moreover, we showed that the characteristic velocity associated with the high-q linear scaling of the relaxation rate corresponds to the typical velocity of bubble displacements in real space. Once normalised with the coarsening rate, this velocity does not exhibit a significant variation within the range of bubble radii investigated, as already pointed out for shaving foam.[24] However, we stress that while shaving foam reaches a self-similar growth regime after a transient time of the order of tens of minutes,[20] our foams are not expected to head towards a scaling state, and, thus, we do not expect this velocity to remain constant indefinitely. In the long run, foamed emulsions indeed deviate from traditional coarsening, eventually breaking Plateau laws.[28] On the other hand, here, we focused on the early stage of coarsening, where possible deviations in the local structure are not enough to impact the bubble size distribution, which is similar at different ϕ and still resembles that of traditional aqueous foams.[27] The global foam structure can hence be considered in first approximation the same, enabling comparisons between the samples.

Furthermore, we shed new light on the link between the bubble dynamics and the rheological properties of the foam continuous phase. We showed that while the characteristic velocity of persistent bubble motion at short length scales is governed by the elastic properties of the interstitial emulsion, emulsion plasticity starts to play a role only at larger length scales. The gradual suppression of mutual bubble rearrangements with increasing emulsion yield stress[27] modifies the slope of the relaxation rate in the low-q regime towards the recovery of a fully linear dispersion relation. This suggests a limiting case in which bubbles keep displacing without rearranging, deforming the foam, and leading to unconventional bubble shapes. However, the existence of a finite emulsion yield stress does not completely impede bubbles from eventually rearranging, preventing the observation of perfectly linear scaling over the whole range of accessible wavevectors q.

Beyond the new results on the structural relaxation of such complex foams, our experimental approach also shows how a tracking-free technique like DDM can be successfully used to extract in-depth information on sample dynamics with simple imaging experiments. This can be of particular interest for foam studies in general, as high-quality bubble segmentation is often impeded by sample turbidity, as well as for studies of soft glassy materials composed of very small elementary constituents, which are typically studied with light, X-rays, and neutron scattering in reciprocal space.

Finally, our work can pave the way for future experiments changing the nature of the foam continuous phase. Extending this to other systems would be of great relevance in establishing a thorough link between matrix rheology and coarsening-related bubble dynamics.

Author contributions

All authors were involved in the conceptualisation of the experimental work. C. G. performed the experiments. F. G. and R. C. designed the methodology. C. G. analysed the data and wrote the original draft. A. S. and F. G. supervised the project. All authors discussed the results and contributed to the final manuscript.

Data availability

The image sequences of the coarsening foams used in this study can be found at **https://zenodo.org/doi/10.5281/zenodo.12759663**.

Conflicts of interest

There are no conflicts to declare.

Acknowledgements

We acknowledge illuminating discussions with Véronique Trappe. This work has been partly supported by Associazione Italiana per la Ricerca sul Cancro (AIRC) to C. G. and F. G. (MFAG#22083).

Notes and references

1 M. Cloitre, R. Borrega and L. Leibler, *Phys. Rev. Lett.*, 2000, **85**, 4819.
2 S. Marze, R.-M. Guillermic and A. Saint-Jalmes, *Soft Matter*, 2009, **5**, 1937–1946.
3 E.-J. Donth, *The glass transition: relaxation dynamics in liquids and disordered materials*, Springer Science & Business Media, 2001, vol. 48.
4 L. Cipelletti and L. Ramos, *J. Phys.: Condens. Matter*, 2005, **17**, R253.

5 L. Ramos and L. Cipelletti, *Phys. Rev. Lett.*, 2001, **87**, 245503.
6 L. Cipelletti, L. Ramos, S. Manley, E. Pitard, D. A. Weitz, E. E. Pashkovski and M. Johansson, *Faraday Discuss.*, 2003, **123**, 237–251.
7 B. Ruta, Y. Chushkin, G. Monaco, L. Cipelletti, E. Pineda, P. Bruna, V. Giordano and M. Gonzalez-Silveira, *Phys. Rev. Lett.*, 2012, **109**, 165701.
8 B. Ruta, G. Baldi, G. Monaco and Y. Chushkin, *J. Chem. Phys.*, 2013, **138**(5), 054508.
9 Z. Evenson, B. Ruta, S. Hechler, M. Stolpe, E. Pineda, I. Gallino and R. Busch, *Phys. Rev. Lett.*, 2015, **115**, 175701.
10 B. Ruta, E. Pineda and Z. Evenson, *J. Phys.: Condens. Matter*, 2017, **29**, 503002.
11 G. Rodriguez-Lopez, K. Martens and E. E. Ferrero, *Phys. Rev. Mater.*, 2023, **7**, 105603.
12 J.-P. Bouchaud and E. Pitard, *Eur. Phys. J. E*, 2001, **6**, 231–236.
13 E. E. Ferrero, K. Martens and J.-L. Barrat, *Phys. Rev. Lett.*, 2014, **113**, 248301.
14 P. Chaudhuri and L. Berthier, *Phys. Rev. E*, 2017, **95**, 060601.
15 M. Bouzid, J. Colombo, L. V. Barbosa and E. Del Gado, *Nat. Commun.*, 2017, **8**, 15846.
16 Z. W. Wu, W. Kob, W.-H. Wang and L. Xu, *Nat. Commun.*, 2018, **9**, 5334.
17 K. Trachenko and A. Zaccone, *J. Phys.: Condens. Matter*, 2021, **33**, 315101.
18 D. Durian, D. Weitz and D. Pine, *J. Phys.: Condens. Matter*, 1990, **2**, SA433.
19 D. Durian, D. Weitz and D. Pine, *Science*, 1991, **252**, 686–688.
20 D. J. Durian, D. A. Weitz and D. J. Pine, *Phys. Rev. A: At., Mol., Opt. Phys.*, 1991, **44**, R7902–R7905.
21 S. Cohen-Addad and R. Höhler, *Phys. Rev. Lett.*, 2001, **86**, 4700.
22 A. S. Gittings and D. J. Durian, *Phys. Rev. E: Stat., Nonlinear, Soft Matter Phys.*, 2008, **78**, 066313.
23 D. A. Sessoms, H. Bissig, A. Duri, L. Cipelletti and V. Trappe, *Soft Matter*, 2010, **6**, 3030–3037.
24 F. Giavazzi, V. Trappe and R. Cerbino, *J. Phys.: Condens. Matter*, 2021, **33**, 24002.
25 M. Le Merrer, S. Cohen-Addad and R. Höhler, *Phys. Rev. Lett.*, 2012, **108**, 188301.
26 M. Le Merrer, S. Cohen-Addad and R. Höhler, *Phys. Rev. E: Stat., Nonlinear, Soft Matter Phys.*, 2013, **88**, 022303.
27 C. Guidolin, E. Rio, R. Cerbino, F. Giavazzi and A. Salonen, *arXiv*, 2024, preprint, DOI: 10.48550/arXiv.2405.09382 [cond-mat.soft].
28 C. Guidolin, J. Mac Intyre, E. Rio, A. Puisto and A. Salonen, *Nat. Commun.*, 2023, **14**(1), 1125.
29 T. G. Mason, J. Bibette and D. A. Weitz, *Phys. Rev. Lett.*, 1995, **75**, 2051–2054.
30 T. G. Mason, J. J. Bibette and D. A. Weitz, *J. Colloid Interface Sci.*, 1996, **179**, 439–448.
31 R. Cerbino and V. Trappe, *Phys. Rev. Lett.*, 2008, **100**, 1–4.
32 M. Pasquet, N. Galvani, O. Pitois, S. Cohen-Addad, R. Höhler, A. T. Chieco, S. Dillavou, J. M. Hanlan, D. J. Durian and E. Rio, *et al.*, *C. R. Mec.*, 2023, **351**, 139–161.
33 M. Pasquet, N. Galvani, A. Requier, S. Cohen-Addad, R. Höhler, O. Pitois, E. Rio, A. Salonen and D. Langevin, *Soft Matter*, 2023, **19**, 6267–6279.
34 J. Goyon, F. Bertrand, O. Pitois and G. Ovarlez, *Phys. Rev. Lett.*, 2010, **104**, 128301.
35 F. Giavazzi, D. Brogioli, V. Trappe, T. Bellini and R. Cerbino, *Phys. Rev. E: Stat., Nonlinear, Soft Matter Phys.*, 2009, **80**, 031403.
36 R. Cerbino, D. Piotti, M. Buscaglia and F. Giavazzi, *J. Phys.: Condens. Matter*, 2017, **30**, 025901.
37 F. Giavazzi, C. Malinverno, G. Scita and R. Cerbino, *Front. Phys.*, 2018, **6**, 120.
38 J.-Y. Tinevez, N. Perry, J. Schindelin, G. M. Hoopes, G. D. Reynolds, E. Laplantine, S. Y. Bednarek, S. L. Shorte and K. W. Eliceiri, *Methods*, 2017, **115**, 80–90.
39 D. Ershov, M.-S. Phan, J. W. Pylvänäinen, S. U. Rigaud, L. Le Blanc, A. Charles-Orszag, J. R. W. Conway, R. F. Laine, N. H. Roy, D. Daria Bonazzi, G. Duménil, G. Jacquemet and J.-Y. Tinevez, *Nat. Methods*, 2022, **19**, 829–832.
40 J. Von Neumann, *Metal Interfaces*, American Society for Metals, Cleveland, 1952, p. 108.
41 W. W. Mullins, *J. Appl. Phys.*, 1986, **59**, 1341–1349.
42 I. Cantat, S. Cohen-Addad, F. Elias, F. Graner, R. Hohler, O. Pitois, F. Rouyer and A. Saint-Jalmes, *Foams. Structure and Dynamics*, Oxford University Press, New York, 2013.
43 M. Kogan, L. Ducloué, J. Goyon, X. Chateau, O. Pitois and G. Ovarlez, *Rheol. Acta*, 2013, **52**, 237–253.
44 F. Gorlier, Y. Khidas and O. Pitois, *J. Colloid Interface Sci.*, 2017, **501**, 103–111.
45 M. Drechsler, F. Giavazzi, R. Cerbino and I. M. Palacios, *Nat. Commun.*, 2017, **8**, 1520.
46 S. Castellini, M. Brizioli, C. Giraudet, M. Carpineti, F. Croccolo, F. Giavazzi and A. Vailati, *Eur. Phys. J. E*, 2024, **47**, 25.
47 L. G. Wilson, V. A. Martinez, J. Schwarz-Linek, J. Tailleur, G. Bryant, P. Pusey and W. C. Poon, *Phys. Rev. Lett.*, 2011, **106**, 018101.
48 C. Rodrguez-Cruz, M. Molaei, A. Thirumalaiswamy, K. Feitosa, V. N. Manoharan, S. Sivarajan, D. H. Reich, R. A. Riggleman and J. C. Crocker, *Soft Matter*, 2023, **19**, 6805–6813.
49 R. Weron, *Int. J. Mod. Phys. C*, 2001, **12**, 209–223.